AIAA JOURNAL
Vol. 31, No. 9, September 1993

Three-Dimensional Time-Marching Aeroelastic Analyses Using an Unstructured-Grid Euler Method

Russ D. Rausch*
Purdue University, West Lafayette, Indiana 47907
John T. Batina†
NASA Langley Research Center, Hampton, Virginia 23681
and
Henry T. Y. Yang‡
Purdue University, West Lafayette, Indiana 47907

Modifications to a three-dimensional, implicit, upwind, unstructured-grid Euler code for aeroelastic analysis of complete aircraft configurations are described. The modifications involve the addition of the structural equations of motion for their simultaneous time integration with the governing flow equations. The paper presents a detailed description of the time-marching aeroelastic procedures and presents comparisons with experimental data to provide an assessment of the capability. Flutter results are shown for an isolated 45-deg swept-back wing and a supersonic transport configuration with a fuselage, clipped delta wing, and two identical rearward-mounted engine nacelles. Comparisons are made between computed and experimental flutter characteristics to assess the accuracy of the aeroelastic results.

Introduction

IN recent years, there has been increased interest in the development of aeroelastic analysis methods involving computational fluid dynamics techniques.[1] This work in the area of computational aeroelasticity has focused on developing finite difference codes for the solution of the transonic small-disturbance[2,3] and full potential equations,[4,5] although growing efforts are under way for the solution of the Euler and Navier-Stokes equations.[6-17] For example, Bendiksen and Kousen[6] presented transonic flutter results for two-degree-of-freedom (plunging and pitching) airfoils by simultaneously integrating the structural equations of motion and the two-dimensional unsteady Euler equations. The Euler equations were discretized in space using a finite volume method on a moving mesh and integrated using a Runge-Kutta time-stepping scheme. The instantaneous mesh was taken to be a superposition of meshes corresponding to rigid plunging and pitching of the airfoil. In a following study, Kousen and Bendiksen[7] applied their method of Ref. 6 to investigate the nonlinear aeroelastic behavior of two-degree-of-freedom airfoils at transonic speeds and showed that transonic flutter instabilities led to stable limit-cycle oscillations involving very large amplitudes. Most recently, Bendiksen[8] presented an alternative approach to the integration of the structural equations of motion and the fluid flow equations. Wu et al.[9] integrated in time the unsteady compressible Navier-Stokes equations for airfoils undergoing one- and two-degree-of-freedom aeroelastic motions. In Ref. 9, flutter characteristics of airfoils at high angles of attack, including cases with stall flutter, were investigated. The method of Ref. 9 also has been applied by Reddy et al.[10] to study the effects of rotational flow, viscosity, thickness, and shape on the transonic flutter dip phenomena. The study concluded that the influence of these effects on flutter, for the cases considered, was small near the minimum of the flutter dip but may be large away from the dip. Guruswamy[11-14] demonstrated simultaneous time integration of the three-dimensional Euler and Navier-Stokes equations along with the structural equations of motion. The inviscid capability first was demonstrated in a time-marching flutter analysis performed for a rectangular wing with a parabolic-arc airfoil section, and the viscous capability was demonstrated later for an aeroelastic deformation of a blended wing body to study shock-vortex interaction. Finally, Robinson et al.[15] presented Euler aeroelastic results for a 45-deg swept-back wing using a deforming mesh capability. A common feature of the aforementioned aeroelastic methods is that all involved algorithms that required a structured computational grid.

As an alternative to structured grid methods, some recent efforts in computational fluid dynamics are directed toward solving the governing flow equations using unstructured grids.[16-28] These grids typically are constructed from triangles in two dimensions, and they consist of an assemblage of tetrahedra in three dimensions. One benefit of using these geometric shapes is that they may be oriented easily to conform to the geometry being considered, making it possible to represent accurately complicated shapes such as multielement airfoils in two dimensions or complete aircraft configurations in three dimensions. Application of the unstructured grid methodology has been demonstrated for multielement airfoils[18,19] and complete aircraft configurations.[20,21] Another benefit of the unstructured grid methodology is that the grid data structure simplifies mesh refinement in regions of high-flow gradients to resolve the physics of the flow more accurately. These adaptive grid methods have been demonstrated for steady and unsteady flows in two dimensions[22-25] and for complex geometries in three dimensions.[26,27] A disadvantage, however, of the unstructured grid methodology is the computational overhead of the indirect addressing used to maintain the grid data structure. For example, the computational work, for steady-state solutions obtained using unstructured grid

Received March 23, 1992; presented as Paper 92-2506 at the AIAA/ASME/ASCE/AHS/ASC 33rd Structures, Structural Dynamics, and Materials Conference, Dallas, TX, April 13-15, 1992; revision received Dec. 8, 1992; accepted for publication Jan. 7, 1993.

*Graduate Research Assistant, School of Aeronautics and Astronautics. Member AIAA.
†Senior Research Scientist, Unsteady Aerodynamics Branch, Structural Dynamics Division. Associate Fellow AIAA.
‡Professor and Dean, Schools of Engineering. Fellow AIAA.

algorithms, has been shown to be 2 to 5 times more expensive than that required to obtain solutions on a structured grid with the same number of cells.[29]

Since there are a number of benefits in using unstructured grid methods, it is appropriate to develop computer codes for transonic aeroelastic analysis of complete aircraft configurations. As a first step, an assessment of the applicability of the unstructured grid methodology for the aeroelastic analysis of airfoils was reported by the present authors in Ref. 16. Comparisons were made with solutions obtained using a structured grid code to determine the accuracy of the unstructured grid methodology. The unstructured grid capability included a deforming mesh algorithm to allow the grid to conform to the instantaneous position of the moving or deforming airfoil under consideration. The algorithm is quite general and necessary for the treatment of realistic motions encountered during an aeroelastic calculation. The conclusion in Ref. 16 was that accurate flutter results could be computed using the unstructured grid methodology. In an independent study by Mortchelewitcz and Sens,[17] three-dimensional unsteady results were presented for a wing undergoing forced harmonic motion. In Ref. 17 comparisons of calculated unsteady pressures were made with experimental data. The capability included the implementation of transpiration boundary conditions that allowed the mesh to remain fixed for unsteady applications where the relative motion of the geometry is assumed small.

The purpose of the present study is to incorporate the aeroelastic analysis procedures of Ref. 16 into a three-dimensional, implicit, upwind Euler scheme on unstructured deforming meshes and to assess the applicability of the unstructured grid methodology for aeroelastic analysis of complete aircraft configurations. The objectives of the research are 1) to develop a solution algorithm for time-accurate unsteady flow calculations on a deforming mesh, 2) to implement the aeroelastic analysis procedures, 3) to compute aeroelastic results for an isolated wing and for a complete aircraft configuration, and 4) to determine the accuracy of the solutions by making comparisons with available experimental data. The eventual goal is to develop a highly accurate and efficient solution algorithm for the Euler and Navier-Stokes equations for aeroelastic analysis of complex aircraft configurations. The paper gives a brief description of the flow solver used in the current effort, a description of the deforming mesh algorithm, and the time-marching aeroelastic analysis procedures. To demonstrate the time-marching aeroelastic procedures that were implemented, flutter results are presented for an isolated 45-deg swept-back wing and a supersonic transport configuration with a clipped delta wing and two rearward-mounted engine nacelles. The authors believe that these are the first three-dimensional flutter calculations obtained using the unstructured-grid methodology. The paper also presents comparisons between computed and experimental flutter characteristics to provide an assessment of the accuracy of the capability.

Upwind-Type Euler Solution Algorithm

The Euler equations are solved using the three-dimensional upwind-type solution algorithm developed by Batina.[28] The solution algorithm of Ref. 28 was extended by Rausch[30] for time-accurate unsteady flow calculations on a deforming mesh and demonstrated for AGARD case 5, proposed by the AGARD Structures and Materials Panel.[31] The algorithm, which is a cell-centered finite volume scheme, uses upwind differencing based on flux-vector splitting,[32] similar to upwind schemes developed for use on structured meshes. The flux-split discretization accounts for the local wave-propagation characteristics of the flow and captures shock waves sharply with at most one grid point within the shock structure. An additional advantage of using flux splitting is that the discretization is naturally dissipative and, consequently, does not require additional artificial dissipation terms or the adjustment of free parameters to control the dissipation. However, in calculations involving a higher order upwind scheme such as this, oscillations in the solution near shock waves are expected to occur. To eliminate these oscillations, flux limiting usually is required. In the present study, a continuously differentiable flux limiter was employed.

The Euler equations are integrated in time using an implicit time-integration scheme involving a Gauss-Seidel relaxation procedure.[28] The relaxation procedure is implemented by reordering the elements that make up the unstructured mesh from upstream to downstream. The solution is obtained by sweeping two times through the mesh as dictated by stability considerations. The first sweep is performed in the direction from upstream to downstream, and the second sweep is from downstream to upstream. For purely supersonic flows, the second sweep is unnecessary. This relaxation scheme is stable for large time steps and thus allows the selection of the step size based on the temporal accuracy of the problem being considered, rather than on the numerical stability of the algorithm. Consequently, very large time steps may be used for rapid convergence to steady state, and an appropriate step size may be selected for unsteady cases, independent of numerical stability issues.

Deforming Mesh Algorithm

A deforming mesh algorithm is used to move the mesh for unsteady calculations where the geometry deforms. The method, as developed in Ref. 33, models the mesh as a spring network where each edge of each tetrahedron represents a spring with a stiffness inversely proportional to the length of that edge. In this procedure, grid points along the outer boundary of the mesh are held fixed, and the instantaneous locations of the points on the wing (inner boundary) are specified. For aeroelastic calculations, the position of the inner boundary is determined by the structural equations of motion. The locations of the interior nodes then are determined by solving the static equilibrium equations that result from a summation of forces at each node in the x, y, and z coordinate directions. The solution of the equilibrium equations is approximated by using a predictor-corrector procedure, which first predicts the new locations of the nodes by extrapolation from grids at previous time levels and then corrects these locations by using several Jacobi iterations of the static equilibrium equations. The predictor-corrector procedure is relatively efficient because of the small number of Jacobi iterations required to move the mesh.

Time-Marching Aeroelastic Analysis

In this section the aeroelastic equations of motion, the time-marching solution procedure, and the modal identification technique are described.

Aeroelastic Equations of Motion

The aeroelastic equations of motion can be written for each mode i as

$$m_i\ddot{q}_i + c_i\dot{q}_i + k_i q_i = Q_i \tag{1}$$

where q_i is the generalized displacement, m_i is the generalized mass, c_i is the generalized damping, k_i is the generalized stiffness, and Q_i is the generalized force computed by integrating the pressure weighted by the mode shapes. These equations of motion are derived by assuming that the deformation of the body under consideration can be described by a separation of variables involving the summation of free vibration modes weighted by generalized displacements. The implementation of the equations of motion is slightly different than that of Refs. 3, 15, and 16. In this development the generalized aerodynamic forces include modal deflections in all three coordinate directions, whereas previous implementations involved deflections only in the vertical direction. It is noted, however, that the results presented herein involve deflections only in the vertical direction.

Time-Marching Solution

The solution procedure for integrating Eq. (1) is similar to that described by Edwards et al.[34,35] A similar formulation is implemented in the present study for multiple degrees of freedom. Here the linear state equations are written as

$$\dot{x}_i = Ax_i + Bu_i \tag{2}$$

where A and B are coefficient matrices that result from the change of variables $x_i = [q_i \dot{q}_i]^T$, and u_i is the nondimensional representation of the generalized force Q_i. Equation (2) is integrated in time using the modified state-transition matrix structural integrator[35] implemented as a predictor-corrector procedure. The prediction for x_i^{n+1}, $\tilde{x}_i^{n+1}$ is given by

$$\tilde{x}_i^{n+1} = \Phi x_i^n + \Theta B(3u_i^n - u_i^{n-1})/2 \tag{3}$$

where Φ is the state-transition matrix and Θ is the integral of the state-transition matrix from time step n to $n+1$. Then, $\tilde{x}_i^{n+1}$ is used to compute the flowfield and evaluate the nondimensional generalized force $\tilde{u}_i^{n+1}$. These values then are used in the corrector step to determine x_i^{n+1}, given by

$$x_i^{n+1} = \Phi x_i^n + \Theta B(\tilde{u}_i^{n+1} + u_i^n)/2 \tag{4}$$

Modal Identification Technique

Damping and frequency characteristics of the aeroelastic responses are estimated from the response curves by using the modal identification technique of Bennett and Desmarais.[36] The modal estimates are determined by a least-squares curve fit of the responses of the form

$$q_i(T) = a_0 + \sum_{j=1}^{m} e^{\sigma_j T}[a_j \cos(\omega_j T) + b_j \sin(\omega_j T)] \quad i = 1, 2, \ldots \tag{5}$$

where m is the number of modes.

Results and Discussion

Flutter results are presented in this section for a 45-deg swept-back wing and for a supersonic transport configuration with a clipped delta wing and two rearward-mounted engine nacelles. The results are used to assess the time-marching aeroelastic capability. The accuracy of the results is determined by making comparisons with available experimental data.

45-Deg Swept-Back Wing

To assess the unstructured-grid code for three-dimensional aeroelastic applications, a simple well-defined wing was selected as a first step toward performing aeroelastic analyses for complete aircraft configurations. The wing that was analyzed was a half-span wind-tunnel-wall-mounted model that has a quarter-chord sweep angle of 45 deg, a panel aspect ratio of 1.65, and a taper ratio of 0.66 (Ref. 37). The wing is an AGARD standard aeroelastic configuration that was tested in the Transonic Dynamics Tunnel (TDT) at NASA Langley Research Center. A plan view of the wing is shown in Fig. 1. The wing has a NACA 65A004 airfoil section that was constructed of laminated mahogany and hence was essentially homogeneous. To obtain flutter for a wide range of flow Mach number and density in the TDT, holes were drilled through the wing to reduce its stiffness. To maintain the aerodynamic shape of the wing, the holes were filled with a rigid foam plastic.

In the aeroelastic analysis, the wing is represented structurally using the first four natural vibration modes that are illustrated in Figs. 2a and 2b. Figure 2a shows oblique projections of the natural modes, whereas Fig. 2b shows the corresponding deflection contours. These modes, which are numbered 1-4, represent first bending, first torsion, second bending, and second torsion, respectively, as determined by a finite element analysis. The modes have natural frequencies

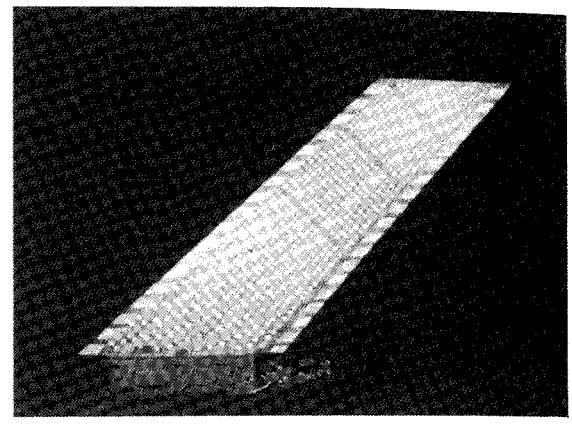

Fig. 1 Plan view of 45-deg swept-back wing model.

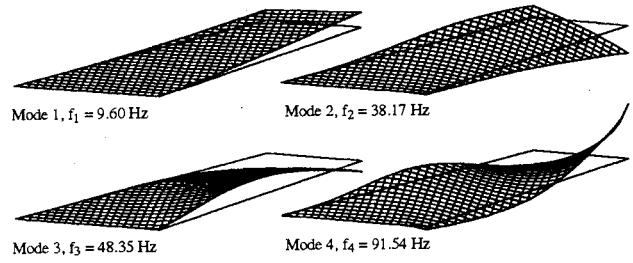

a) Oblique projections

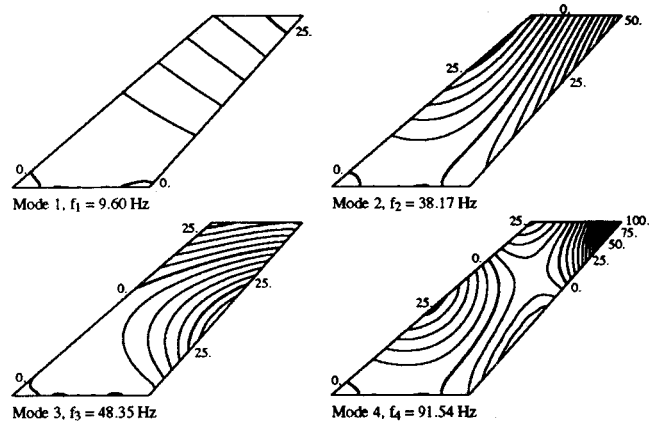

b) Deflection contour lines

Fig. 2 Natural vibration modes of the 45-deg swept-back wing.

that range from 9.6 Hz for the first bending mode to 91.54 Hz for the second torsion mode.

The 45-deg swept-back wing was modeled aerodynamically using an unstructured mesh generated by an advancing front method that is part of the VGRID3D[38] software package. The computational mesh extends two wing semispans from the symmetry plane in the span direction. Also, the mesh extends 10 root chord lengths above/below and upstream/downstream of the wing surface to rectangular outer boundaries. The meshes on the upper and lower surfaces of the wing are shown in Fig. 3, which indicates that cells have been clustered near the leading edge of the wing. The leading edge is a region of large flow gradients, and the clustered cells produce a more accurate calculation of the leading-edge surface pressure. Figure 4 shows a partial view of the plane of symmetry and the wing. In this figure the mesh along the symmetry plane shows how the cells are stretched away from the wing. The complete mesh contains 129,746 tetrahedra and 23,727 nodes.

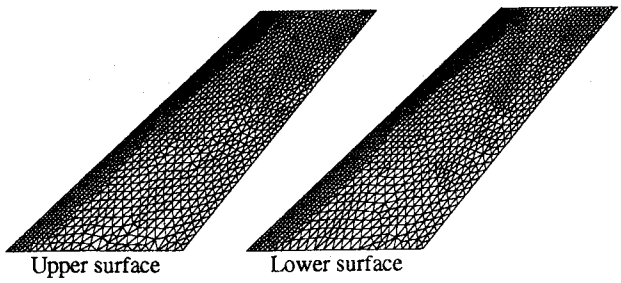

Fig. 3 Surface mesh for the 45-deg swept-back wing.

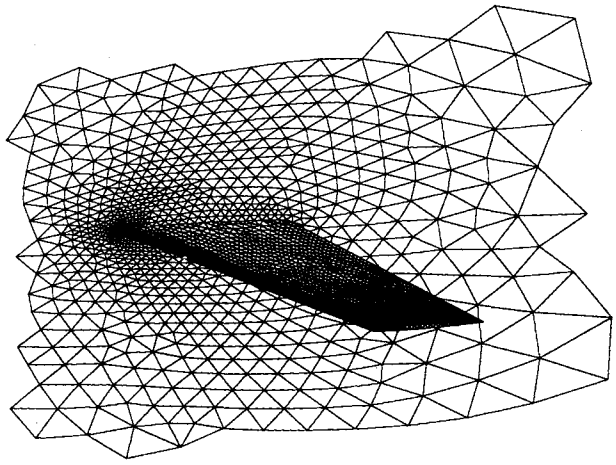

Fig. 4 Partial view of the surface mesh for the symmetry plane and the 45-deg swept-back wing.

Flutter characteristics were calculated for comparison with measured values of the flutter speed index and the nondimensional flutter frequency at freestream Mach numbers M_∞ of 0.499, 0.678, 0.901, and 0.960 at 0-deg angle of attack. The calculation of each flutter point was started by obtaining a steady-rigid solution at the aforementioned flow conditions. Typically, the next step is to compute a static-aeroelastic solution. However, for these steady-state flow conditions the wing does not deflect statically since the wing is symmetric and at 0-deg angle of attack. Therefore, once the steady-rigid solution was obtained for each Mach number, a dynamic-aeroelastic calculation was started by perturbing the first two structural modes with initial velocity conditions. To bracket the flutter point, time-marching calculations were performed for several values of dynamic pressure, $(\frac{1}{2}\rho_\infty U_\infty^2)_{calc}$, nondimensionalized by the experimental flutter dynamic pressure, $(\frac{1}{2}\rho_\infty U_\infty^2)_{exp}$, including $(\frac{1}{2}\rho_\infty U_\infty^2)_{calc}/(\frac{1}{2}\rho_\infty U_\infty^2)_{exp}$ of 0.7, 0.8, 0.9, 1.0, and 1.1. In general, each calculation, at a specific value of dynamic pressure, required approximately 9000 time steps to obtain three cycles of motion of the dominant flutter mode. This required approximately 41.3 h of CPU time and about 40 Mw of memory on the Cray-2s computer at the NASA Langley Research Center.

The aeroelastic responses that result from the dynamic-aeroelastic calculation were analyzed using the method of Ref. 36 for their damping and frequency components. These components, along with their corresponding value of dynamic pressure, were interpolated to zero damping of the dominant flutter mode to obtain the flutter point. Figure 5 shows comparisons of computed flutter characteristics with experimental data. Plots of flutter speed index $U_\infty/b\omega_\alpha\sqrt{\mu}$ and nondimensional flutter frequency ω/ω_α as a function of freestream Mach number are shown in Figs. 5a and 5b, respectively. The experimental flutter data defines a typical transonic flutter "dip" with the bottom near $M_\infty = 1.0$ for this wing. The bottom of the dip in flutter speed index (Fig. 5a) was defined by the approach to the $M_\infty = 1.072$ flutter point during the wind-tunnel operation. Results from the Euler code are presented at the values of M_∞ at which the flutter data were measured. In the Mach number range considered in this study ($0.499 \le M_\infty \le 0.96$), a conservative flutter speed was computed at all four Mach numbers in comparison with the experimental data. In general the computed results agree well with experimental data at $M_\infty = 0.499$ and 0.678 in flutter speed index and in frequency ratio. Near the transonic flutter dip, however, the computed results deviate from the data for the flutter speed index but show fair agreement in flutter frequency ratio. The flutter results presented earlier are believed by the authors to be the first three-dimensional flutter results obtained using the unstructured-grid methodology.

Supersonic Transport Configuration

To assess the code for complete aircraft aeroelastic applications, a calculation was performed for a complex configuration. This configuration represents an increase in complexity from that of the 45-deg swept-back wing from the standpoint of the increased complexity of the geometry and the natural vibration modes. The configuration analyzed was a half-span model of an early supersonic transport (SST) configuration that was tested in heavy gas in the NASA Langley TDT.[39,40] This configuration consisted of a rigid fuselage and a flexible clipped delta wing with two rearward-mounted simulated engine nacelles. A view of the model mounted in the TDT is presented in Fig. 6. The wing that is analyzed in this paper is that denoted as wing C in Ref. 39. The wing has a leading-edge sweep angle of 50.5 deg, a panel aspect ratio of 1.24, and a taper ratio of 0.142. The airfoil section is a circular arc with a

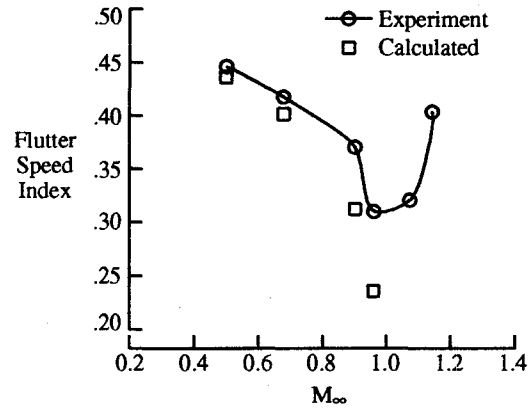

a) Flutter speed index

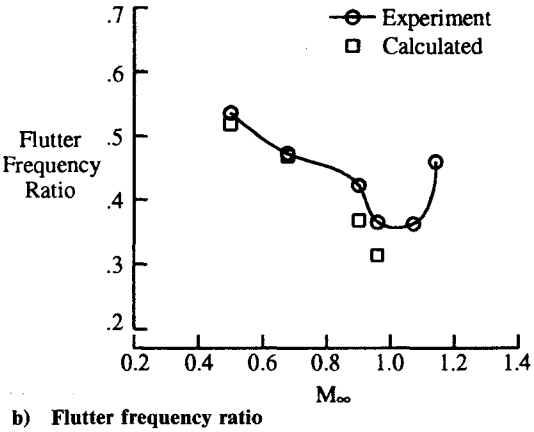

b) Flutter frequency ratio

Fig. 5 Comparisons of Euler flutter predictions with experimental data for the 45-deg swept-back wing.

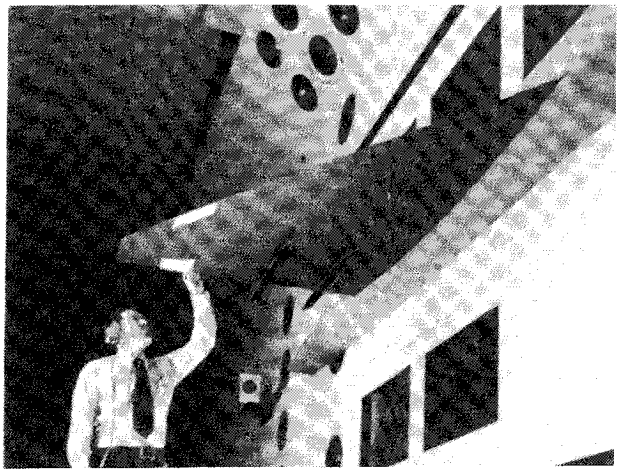

Fig. 6 Supersonic transport model with clipped delta wing in the NASA Langley Transonic Dynamics Tunnel.

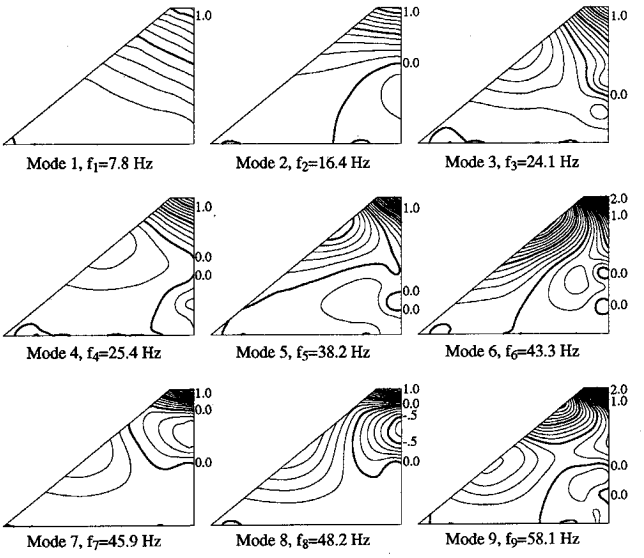

Fig. 7 Deflection contours of the natural vibration modes for the clipped delta wing of the supersonic transport model.

maximum thickness-to-chord ratio of 0.03. The wing was constructed of a load-carrying aluminum-alloy plate structure with cutouts chemically milled to simulate a beam structure and was covered with balsa wood that was contoured to the desired airfoil shape. The wing was clamped to a relatively rigid mounting block that was attached to a turntable on the tunnel wall. This mounting arrangement isolated the wing vibrations to the turntable and prevented structural interaction between the wing and fuselage. The model also had two identical slender underwing bodies to simulate engine nacelles. Each nacelle consisted of a cylindrical centerbody with an ogive nose section and a conical tail fairing. The total mass of the nacelles was about the same as the total mass of the wing. The fuselage fairing was a half-body of revolution that was extended from the tunnel wall to ensure that the wing root was outside the tunnel wall's boundary layer (Fig. 6).

Nine natural vibration modes and their associated generalized masses were measured.[39] Deflection contours of these wing modes are shown in Fig. 7. The modes have natural frequencies that range from 7.8 Hz for mode 1 to 58.1 Hz for mode 9. The nacelle masses have a large effect on the mode shapes, as shown in Fig. 7, particularly in the inboard region of the wing.

The SST configuration also was modeled using the VGRID3D mesh generation package. The mesh extends two wing semispans from the symmetry plane in the span direction. Also, the mesh extends 10 root chord lengths above/below and upstream/downstream of the wing surface to rectangular outer boundaries. The top, bottom, and side views of the surface mesh of the configuration are shown in Fig. 8. The upper and lower views of the surface mesh show that cells have been clustered near the wing tip and around the nacelles. The side view shows that the wing is placed below the centerline of the fuselage. The complete mesh for the supersonic transport contains 323,818 tetrahedra and 59,429 nodes.

The measured natural vibration mode shapes are interpolated to the surface mesh of the configuration of Fig. 8. The interpolated mode shapes of the configuration are shown in Fig. 9 along with the corresponding natural frequencies. Figure 9 illustrates the relative vertical motion of the clipped delta wing and nacelles with respect to the rigid fuselage. Similar to the model in the wind-tunnel test, the fuselage was rigid as shown in Fig. 9. It should be noted, however, that the time-marching aeroelastic capability allows for general motion of the complete configuration and is *not* restricted to simple wing deflections.

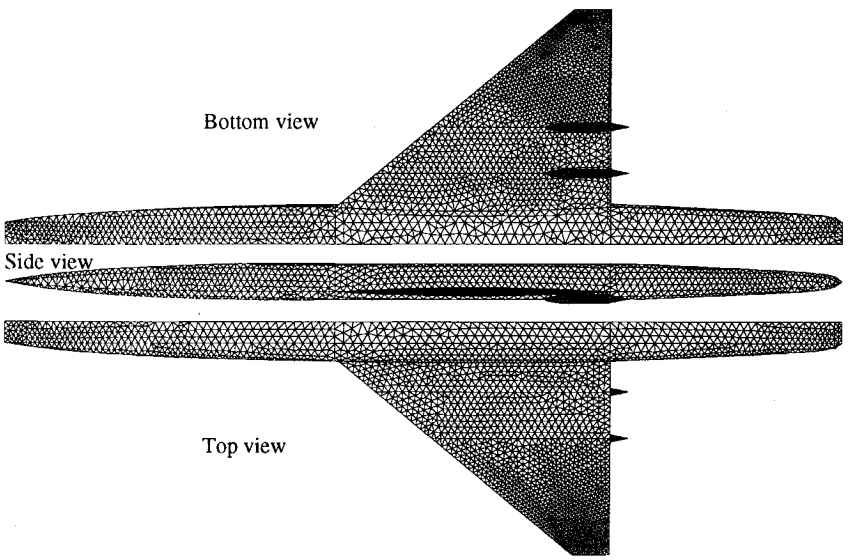

Fig. 8 Surface mesh of the supersonic transport configuration with a clipped delta wing and two rearward-mounted nacelles.

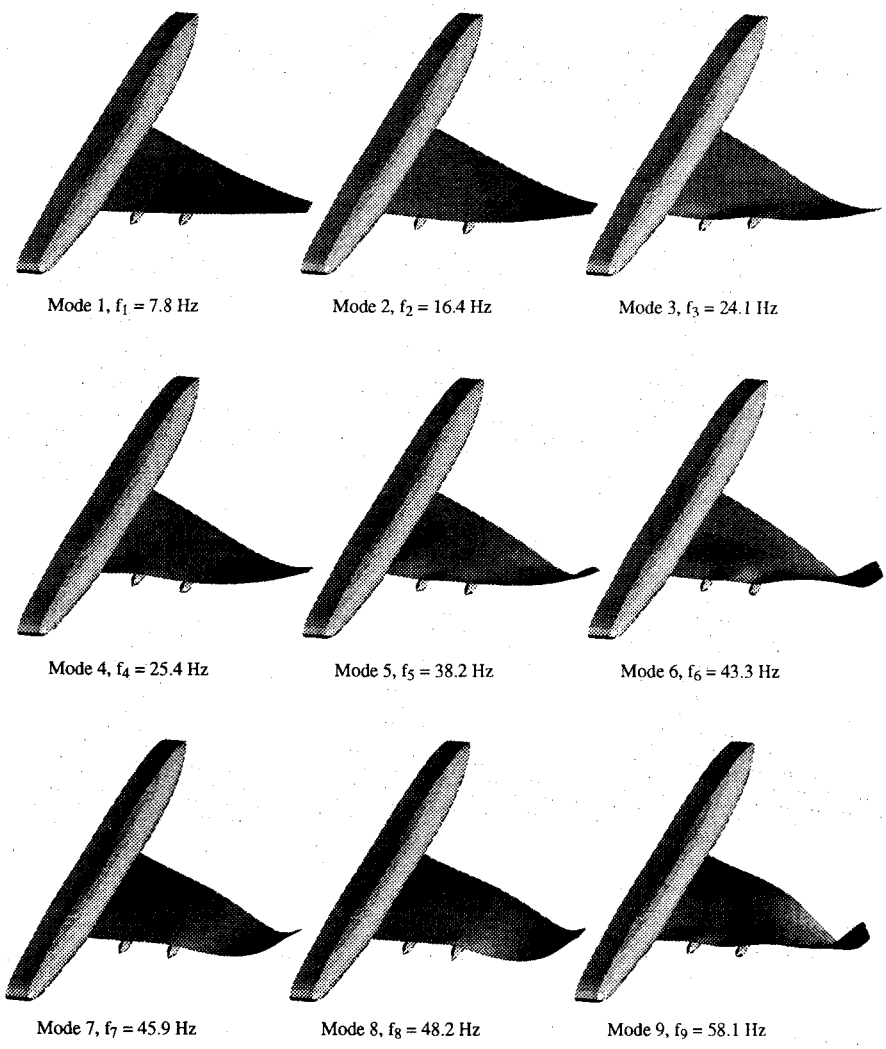

Fig. 9 Natural vibration mode shapes of the supersonic transport configuration with a clipped delta wing and two rearward-mounted nacelles.

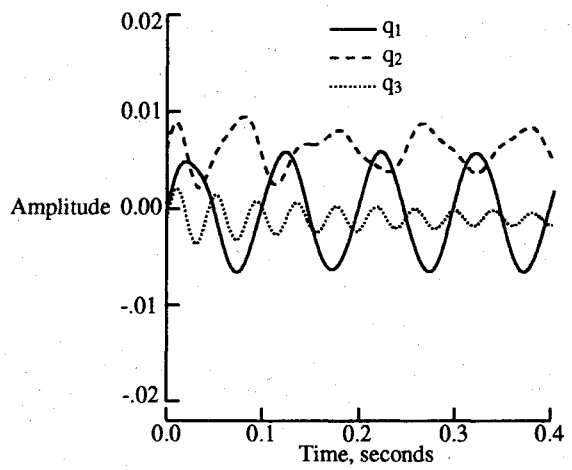

Fig. 10 Generalized displacements at $(\frac{1}{2}\rho_\infty U_\infty^2)_{calc}/(\frac{1}{2}\rho_\infty U_\infty^2)_{exp} = 1.0$ for the supersonic transport configuration at $M_\infty = 0.907$ and 0-deg angle of attack.

A calculation was performed for the SST configuration at $M_\infty = 0.907$ and 0-deg angle of attack. The aeroelastic calculation was performed by first obtaining a steady-rigid solution at these flow conditions. Next a static-aeroelastic solution, during which the wing was allowed to deform due to the aerodynamic loads caused by the nonsymmetric geometry, was computed. To allow rapid convergence of the wing to its static deformed shape and to prevent the wing from oscillating, structural damping was added. Finally a dynamic-aeroelastic calculation was started from the static-aeroelastic solution by perturbing the first three structural modes with initial velocity conditions. Figure 10 shows the resulting generalized displacements for the first three structural modes, where a value of dynamic pressure that was found experimentally to correspond to flutter was used. The first three component modes of the second generalized displacement are shown in Fig. 11. Damping and frequency estimates of the three modes are listed in Table 1. The near neutrally stable mode 1 of the generalized displacement indicates the computed aeroelastic transient is near the flutter point. The calculated flutter frequency was found to be 10 Hz, which compares with the experimental flutter frequency of 11 Hz. The aeroelastic calculation described earlier required approximately 112 h of CPU time and 98 Mw of memory on the Cray-2 computer at the Numerical Aerodynamic Simulation facility located at the

Table 1 Component mode damping and frequencies of the aeroelastic system at $(\frac{1}{2}\rho_\infty U_\infty^2)_{calc}/(\frac{1}{2}\rho_\infty U_\infty^2)_{exp} = 1.0$ for the supersonic transport configuration at $M_\infty = 0.907$ and 0-deg angle of attack

	ζ	ω, Hz
Mode 1	0.002	10.06
Mode 2	0.082	16.04
Mode 3	0.027	24.08

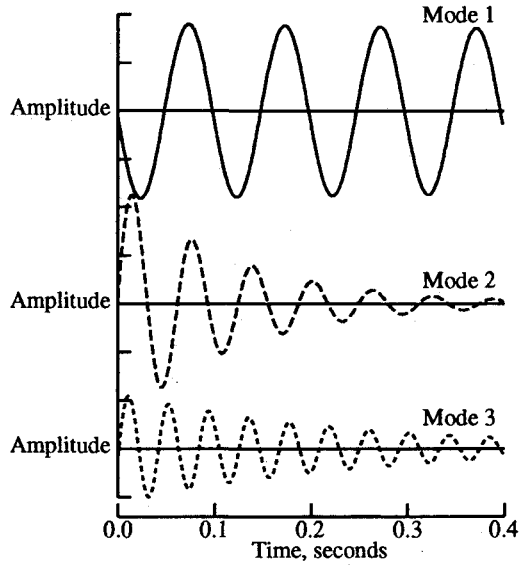

Fig. 11 First three component modes of the second generalized displacement at $(\frac{1}{2}\rho_\infty U_\infty^2)_{calc}/(\frac{1}{2}\rho_\infty U_\infty^2)_{exp} = 1.0$ for the supersonic transport configuration at $M_\infty = 0.907$ and 0-deg angle of attack.

NASA Ames Research Center. The total number of CPU hours consists of approximately 27.2 h for the steady solution (2000 iterations), 30.2 h for the static-aeroelastic solution (2000 time steps), and 54.3 h for the dynamic-aeroelastic solution (3600 time steps).

Concluding Remarks

Modifications to a three-dimensional, implicit, upwind Euler code based on unstructured grids for the aeroelastic analysis of complete aircraft configurations were described. The modifications involved the addition of the structural equations of motion for their simultaneous time integration with the governing flow equations. The flow solver of the Euler code, which is a cell-centered finite volume scheme, uses upwind differencing based on flux-vector splitting and involves an implicit time-integration scheme that uses a Gauss-Seidel relaxation procedure. The code also includes a deforming mesh algorithm that is capable of moving the mesh for general aeroelastic motions of complete aircraft configurations. Flutter results were presented for an isolated 45-deg swept-back wing and a supersonic transport configuration with a clipped delta wing and two rearward-mounted engine nacelles to assess the time-marching aeroelastic procedures that were implemented. Flutter results in the subsonic speed range for the 45-deg swept-back wing agreed well with the experimental flutter characteristics, giving confidence in the accuracy of the aeroelastic capability. However, the flutter results deviated from the experimental flutter characteristics in the transonic speed range, where the solution was believed to be sensitive to mesh spacing. A time-marching aeroelastic calculation was performed for the SST configuration at the value of dynamic pressure that was found experimentally to correspond to flutter. This value of dynamic pressure produced an aeroelastic transient that contained a component mode that was close to being neutrally stable, indicating that the calculated transient was near the flutter point. The frequency of the near neutrally stable component mode was within 10% of the experimental flutter frequency. The authors believe these are the first three-dimensional flutter calculations obtained using the unstructured-grid methodology.

Acknowledgments

The work constitutes a part of the first author's Ph.D. thesis at Purdue University and was supported by the NASA Graduate Student Researchers program under Grant NGT-50406. The authors acknowledge Paresh Parikh and Shahyar Pirzadeh of ViGYAN, Inc., Hampton, Virginia, for providing the grid generation program that was used to generate the three-dimensional grids in the present study.

References

[1]Edwards, J. W., and Malone, J. B., "Current Status of Computational Methods for Transonic Unsteady Aerodynamic and Aeroelastic Applications," NASA TM 104191, Dec. 1991.

[2]Borland, C. J., and Rizzetta, D. P., "Nonlinear Transonic Flutter Analysis," *AIAA Journal,* Vol. 20, No. 11, 1982, pp. 1606–1615.

[3]Batina, J. T., Seidel, D. A., Bland, S. R., and Bennett, R. M., "Unsteady Transonic Flow Calculations for Realistic Aircraft Configurations," *Journal of Aircraft,* Vol. 26, No. 1, 1989, pp. 21–28.

[4]Isogai, K., and Suetsuga, K., "Numerical Simulation of Transonic Flutter of a Supercritical Wing," National Aerospace Lab., TR-276T, Tokyo, Japan, Aug. 1982.

[5]Ide, H., and Shankar, V. J., "Unsteady Full Potential Aeroelastic Computations for Flexible Configurations," AIAA Paper 87-1238, June 1987.

[6]Bendiksen, O. O., and Kousen, K. A., "Transonic Flutter Analysis Using the Euler Equations," AIAA Paper 87-0911, April 1987.

[7]Kousen, K. A., and Bendiksen, O. O., "Nonlinear Aspects of the Transonic Aeroelastic Stability Problem," AIAA Paper 88-2306, April 1988.

[8]Bendiksen, O. O., "A New Approach to Computational Aeroelasticity," AIAA Paper 91-0939, April 1991.

[9]Wu, J., Kaza, K. R. V., and Sankar, L. N., "Technique for the Prediction of Airfoil Flutter Characteristics in Separated Flow," *Journal of Aircraft,* Vol. 26, No. 2, 1989, pp. 168–177.

[10]Reddy, T. S. R., Srivastava, R., and Kaza, K. R. V., "The Effects of Rotational Flow, Viscosity, Thickness, and Shape on Transonic Flutter Dip Phenomena," AIAA Paper 88-2348, April 1988.

[11]Guruswamy, G. P., "Time-Accurate Unsteady Aerodynamic and Aeroelastic Calculations of Wings Using Euler Equations," AIAA Paper 88-2281, April 1988.

[12]Guruswamy, G. P., "Vortical Flow Computations on Swept Flexible Wings Using Navier-Stokes Equations," *AIAA Journal,* Vol. 28, No. 12, 1990, pp. 2077–2084.

[13]Guruswamy, G. P., "Navier-Stokes Computations on Swept-Tapered Wings, Including Flexibility," *Journal of Aircraft,* Vol. 29, No. 4, 1992, pp. 588–597.

[14]Guruswamy, G. P., "Vortical Flow Computations on a Flexible Blended Wing-Body Configuration," *AIAA Journal,* Vol. 30, No. 10, 1992, pp. 2497–2503.

[15]Robinson, B. A., Batina, J. T., and Yang, H. T. Y., "Aeroelastic Analysis of Wings Using the Euler Equations with a Deforming Mesh," *Journal of Aircraft,* Vol. 28, No. 11, 1991, pp. 781–788.

[16]Rausch, R. D., Batina, J. T., and Yang, H. T. Y., "Euler Flutter Analysis of Airfoils Using Unstructured Dynamic Meshes," *Journal of Aircraft,* Vol. 27, No. 5, 1990, pp. 436–443.

[17]Mortchelewitcz, G. D., and Sens, A. S., "Solution of 3-D Euler Equations with Unstructured Meshes for Aeroelasticity Problems," International Forum on Aeroelasticity and Structural Dynamics 1991, TP 1991-62, June 1991.

[18]Mavriplis, D. J., "Multigrid Solution of the 2-D Euler Equations on Unstructured Triangular Meshes," *AIAA Journal,* Vol. 26, No. 7, 1988, pp. 824–831.

[19]Morgan, K., Peraire, J., Thareja, R. R., and Stewart, J. R., "An Adaptive Finite Element Scheme for the Euler and Navier-Stokes Equations," AIAA Paper 87-1172, June 1987.

[20]Jameson, A., Baker, T. J., and Weatherill, N. P., "Calculation of Inviscid Transonic Flow Over a Complete Aircraft," AIAA Paper 86-0103, Jan. 1986.

[21]Peraire, J., Peiro, J., Formaggia, L., Morgan, K., Zienkiewicz, O. C., "Finite Element Euler Computations in Three Dimensions," *International Journal for Numerical Methods in Engineering,* Vol. 26, No. 10, 1988, pp. 2135–2159.

[22]Löhner, R., "The Efficient Simulation of Strongly Unsteady Flows by the Finite Element Method," AIAA Paper 87-0555, Jan. 1987.

[23]Löhner, R., "An Adaptive Finite Element Solver for Transient Problems with Moving Bodies," *Computers and Structures,* Vol. 30, No. 1/2, 1988, pp. 303–317.

[24]Baum, J. D., and Löhner, R., "Numerical Simulation of Shock-Elevated Box Interaction Using an Adaptive Finite-Element Shock Capturing Scheme," AIAA Paper 89-0653, Jan. 1989.

[25]Rausch, R. D., Batina, J. T., and Yang, H. T. Y., "Spatial Adap-

tation of Unstructured Meshes for Unsteady Aerodynamic Flow Computations," *AIAA Journal,* Vol. 30, No. 5, 1992, pp. 1243–1251.

[26]Löhner, R., "Adaptive H-Refinement on 3-D Unstructured Grids for Transient Problems," AIAA Paper 89-0365, Jan. 1989.

[27]Löhner, R., and Baum, J. D., "Numerical Simulation of Shock Interaction with Complex Geometry Three-Dimensional Structures Using a New Adaptive H-Refinement Scheme on Unstructured Grids," AIAA Paper 90-0700, Jan. 1990.

[28]Batina, J. T., "Three-Dimensional Flux-Split Euler Schemes Involving Unstructured Dynamic Meshes," AIAA Paper 90-1649, June 1990.

[29]Salas, M. D. (ed.), *Accuracy of Unstructured Grid Techniques Workshop,* (NASA Langley Research Center, Hampton, VA), Jan. 17, 18, 1990 (NASA Conference Proceedings to be published).

[30]Rausch, R. D., "Time-Marching Aeroelastic and Spatial Adaptation Procedures on Triangular and Tetrahedral Meshes Using an Unstructured-Grid Euler Method," Ph.D. Thesis, Purdue Univ., West Lafayette, IN, Dec. 1992.

[31]Bland, S. R. (compiler), "AGARD Two-Dimensional Aeroelastic Configurations," AGARD-AR-156, Aug. 1979.

[32]Van Leer, B., "Flux-Vector Splitting for the Euler Equations," *Vol. 170 of Lecture Notes in Physics,* Springer-Verlag, Berlin, 1982, pp. 507–512.

[33]Batina, J. T., "Unsteady Euler Algorithm with Unstructured Dynamic Mesh for Complex-Aircraft Aerodynamic Analysis," *AIAA Journal,* Vol. 29, No. 3, 1991, pp. 327–333.

[34]Edwards, J. W., Bennett, R. M., Whitlow, W., Jr., and Seidel, D. A., "Time-Marching Transonic Flutter Solutions Including Angle-of-Attack Effects," *Journal of Aircraft,* Vol. 20, No. 11, 1983, pp. 899–906.

[35]Edwards, J. W., Bennett, R. M., Whitlow, W., Jr., and Seidel, D. A., "Time-Marching Transonic Flutter Solutions Including Angle-of-Attack Effects," AIAA Paper 82-3685, May 1982.

[36]Bennett, R. M., and Desmarais, R. N., "Curve Fitting of Aeroelastic Transient Response Data with Exponential Functions," *Flutter Testing Techniques,* NASA SP-415, May 1975, pp. 43–58.

[37]Yates, E. C., Jr., Land, N. S., and Foughner, J. T., Jr., "Measured and Calculated Subsonic and Transonic Flutter Characteristics of a 45° Sweptback Wing Planform in Air and in Freon-12 in the Langley Transonic Dynamics Tunnel," NASA TN D-1616, March 1963.

[38]Parikh, P., Pirzadeh, S., and Löhner, R., "A Package for 3-D Unstructured Grid Generation, Finite-Element Flow Solution and Flow Field Visualization," NASA CR-182090, Sept. 1990.

[39]Sandford, M. C., Ruhlin, C. L., and Abel, I., "Transonic Flutter Study of a 50.5-Deg Cropped-Delta Wing with Two Rearward-Mounted Nacelles," NASA TN D-7544, June 1974.

[40]Sandford, M. C., Abel, I., and Gray, D. L., "Development and Demonstration of a Flutter-Suppression System Using Active Controls," NASA TR R-450, Dec. 1975.